

ASME Journal of Manufacturing Science and Engineering Online journal at:

https://asmedigitalcollection.asme.org/manufacturingscience



Fengfeng Zhou

School of Mechanical Engineering, Purdue University, 585 Purdue Mall, West Lafayette, IN 47907-2088 e-mail: zhou966@purdue.edu

Xingyu Fu

School of Mechanical Engineering, Purdue University, 585 Purdue Mall, West Lafayette, IN 47907-2088 e-mail: fuxingyu@alumni.purdue.edu

Siying Chen

School of Mechanical Engineering, Purdue University, 585 Purdue Mall, West Lafayette, IN 47907-2088 e-mail: chen2122@purdue.edu

Changheon Han

School of Mechanical Engineering, Purdue University, 585 Purdue Mall, West Lafayette, IN 47907-2088 e-mail: han711@purdue.edu

Martin B. G. Jun'

School of Mechanical Engineering, Purdue University, 585 Purdue Mall, West Lafayette, IN 47907-2088 e-mail: mbgjun@purdue.edu

Three-Dimensional Profile Reconstruction and Internal Defect Detection of Silicon Wafers Using Cascaded Fiber Optic Fabry-Pérot Interferometer and Leaky Field Detection Technologies

Wafer quality control is one of the important processes to improve the yield rate of semiconductor products. Profile quality and defects in the wafer are two key factors that should be taken into consideration. In this research, we introduce a method that measures the profile of the upper surface and the thickness of the wafer at the same time using an optical fiber cascaded Fabry–Pérot interferometer working at wavelength of 1550 nm. Therefore, the 3D profile of the wafer can be reconstructed directly. Testing results show that both accuracy and precision of the Fabry–Pérot interferometer are within a nanometer scale. Defects, especially those embedded inside the wafer, will be detected by monitoring the leaky field with treating wafers as slab waveguides. With the leaky field detection, defects on the lower surface of the wafer were successfully detected by monitoring the leaky field above the upper surface of the wafer. Compared with traditional methods such as radiographic testing or computed tomography testing, the proposed methods provide a cost-effective alternative for wafer quality evaluation. [DOI: 10.1115/1.4065523]

Keywords: wafer inspection, wafer topography, wafer defect detection, interferometer, semiconductor manufacturing, sensors

1 Introduction

After stepping into the information era, semiconductor devices have become the key for information exchange. Silicon is widely used in semiconductor industries due to its excellent material properties. Therefore, quality control of silicon wafers becomes important to produce high-performance devices. In order to produce high-quality wafers, wafer metrology [1] and inspection [2] methods have been developed. The 3D profile provides the geometric quality of a wafer, and wafers with a poor geometric quality will introduce an increase of defective dies [3]. Traditionally, stylus probes, capacitance probes, optical interferometers, microscopes, etc., are used to monitor the distance between the probe and the wafer surface [4]. Stylus probes have a high resolution and long working distance. However, this method is based on the mechanical contact between the stylus tip and the surface of the wafer. Therefore, mechanical deformation of the tip will cause measurement errors and

may also introduce damage to the wafer [5]. The mechanical contact

Due to their unique advantages such as high sensitivity, compactness, high accuracy and precision, optical fiber sensors have been applied to different applications [7–12]. Among them, the fiber optic Fabry–Pérot interferometer (FPI) is popular due to its well-developed theory and simple structure. Nowadays, FPIs have been applied in material science [13], manufacturing [14,15], biology [16–18], and physics [19–21]. Optical fibers operating at 1550 nm wavelengths have been widely applied in optical

Manuscript received October 4, 2023; final manuscript received May 1, 2024; published online June 3, 2024. Assoc. Editor: ChaBum Lee.

principle also limits the measurement speed without losing accuracy. Capacitance probes are based on the capacitance change with the change of distance between the probe and the wafer surface. Oh and Lee [6] developed a capacitance-based sensor by putting the wafer between the two electrodes to measure the capacitance change due to the thickness variation of the wafer. However, this method only measures the thickness of the wafer, but the surface profile still cannot be determined. Visible range light source has also been widely used for wafer surface topography. However, since the extinction coefficient of silicon in visible range has a high value, silicon is nontransparent to visible light and therefore 3D reconstruction requires multiple measurements.

¹Corresponding author.

communication networks and are commercially available. Considering the extinction coefficient of silicon at this wavelength is extremely small, silicon is transparent to light at 1550 nm with a low loss. Therefore, it is possible to reconstruct the 3D profile of a silicon wafer and inspect its internal structure.

In this research, we introduce a method that measures the topography of the wafer surface facing the sensing probe and the thickness of the wafer simultaneously. Therefore, the 3D profile of the wafer can be reconstructed by one single measurement. Due to the high sensitivity of the fiber optic FPI, the resolution reaches to 1 nm and can be even improved with a spectrometer with higher wavelength resolution. We will also introduce a method to detect internal defects that are invisible by surface inspections. A beam of laser at 1550 nm will be guided into the wafer and propagates as the guiding mode. The leaky field caused by defects will be detected by an external detection optical fiber. The surface defects can also be detected with the same approach. Combine the 3D reconstruction technique and the defect detection technique introduced in this research, a complete reconstruction of the wafer structure is possible.

2 Method

2.1 3D Reconstruction. Optical fiber FPIs will be used to reconstruct the 3D profile of the wafer by measuring the topography of one surface of the wafer and the thickness at the same time. A single-mode optical fiber (SMF) working at 1550 nm consists of a core usually with a radius of 4.5 μ m and a cladding with a radius of 62.5 μ m. The refractive index of the core is slightly higher than that of the cladding. The light will be guided inside the core and propagates along the fiber axis. Figure 1 shows the structure of an optical fiber, light can propagate along both directions of the fiber along the fiber axis.

An FPI consists of two reflection surfaces that are placed parallel to each other. A beam of light with a broadband wavelength will propagate between the two mirrors in a direction perpendicular to the surfaces of the two mirrors. This beam of light will be reflected between the mirrors for multiple times. By measuring the spectrum of the light, the optical distance, which is the geometric distance times the refractive index of the medium between the mirrors, can be determined. Figure 2 shows the structure of an FPI, as we can see, the light propagates along the core of the fiber toward the end of the fiber. The interface between the core and the medium forms the first reflection interface labeled as reflection interface 1. After reaching this interface, part of the light will propagate through it to medium due to the transmission and the rest will be reflected into the core. The light that enters the medium will propagate until it hits reflection interface 2 and will be reflected into medium along the opposite direction. Due to the reflection of the two reflection interfaces, the light will be reflected between them back and forth multiple times. Considering the wave property of light, the light between the interfaces will interfere with themselves. Light with some wavelengths will interfere constructively and therefore the corresponding intensity will increase. And light with wavelengths that interfere destructively will have a lower intensity. Therefore, maximums (peaks) and minimums (dips) can be observed in the interference spectrum. The peaks and dips are determined by the optical distance between the two reflection interfaces.

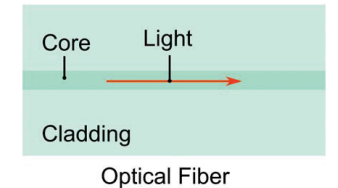


Fig. 1 Structure of a bare optical fiber

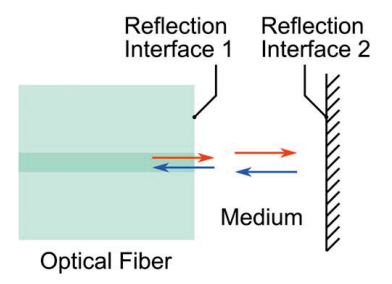


Fig. 2 Structure of a fiber optic FPI

Therefore, when the refractive index of the medium is known, the geometric distance can be determined by the interference spectrum.

References [15] and [22] gave the analytical solution of an FPI. As shown in Fig. 3(a), the electric field of the incident light $E_{\rm inc}$ will be divided into the transmission light $E_{\rm laun}$ and the reflection light $E_{\rm refl,1}$. The transmission light $E_{\rm laun}$ will be reflected between the interfaces. Due to the balance between the gain and the loss between the interfaces, light with a stable intensity will propagate forward (along the direction of the $E_{\rm inc}$) as $E_{\rm circ}$ and backward as $E_{\rm b-circ}$. Similarly, a beam of light with stable amplitude will propagate through the interface between core and medium as $E_{\rm back}$. The total reflection of the light will be a combination of $E_{\rm refl,1}$ and $E_{\rm back}$, labeled as $E_{\rm refl}$. And therefore, we have

$$E_{\text{refl}} = \left[r_1 + \frac{r_2 t_1^2 \exp(-j2\phi)}{1 - r_1 r_2 \exp(-j2\phi)} \right] E_{\text{inc}}$$
 (1)

where r_i is the reflection coefficient of reflection interface i, t_i is the transmission coefficient of reflection interface i, and $2\phi = 2 \times (2\pi dn/\lambda_0)$ is the phase change of the light when travel for a round-trip between the two interfaces. d is the geometric distance between the two reflection interfaces, n is the refractive index of medium, and λ_0 is the wavelength of light in vacuum. j is the imaginary unit. Figure 3(b) shows a typical experimental spectrum of an FPI. As we can see, multiple peaks and dips can be seen due to constructive interference and destructive interference, respectively.

When there are three reflection surfaces aligned perpendicular to the propagation direction of light, a cascaded FPI is formed. Figure 4(a) shows an example of a cascaded FPI. As we can see, it is a combination of two FPIs formed by reflection interface 1, 2 and reflection interface 2, 3. Due to the weak reflectance (3.3%) of reflection interface 1, which is the interface between core and air in this research, the coupling between two FPIs is weak, and we can treat them independently. In this case, the reflection spectrum is a superposition of the two FPIs which gives the optical distances between reflection interface 1 and 2 and reflection interface 2 and 3.

Refractive index reflects the atomic and molecular structure of a material. It is a complex number that describes how light will interact with the material. The real part of refractive index describes the refraction of the material to light. And the imaginary part, which is also called the extinction coefficient, describes how light energy decays inside the material. Let complex refractive index of a material be n' = n + jk where n and k are real numbers. Then the electromagnetic wave becomes

$$E = \mathbf{E}_0 \exp\left[j(n'\mathbf{k}_0 \cdot \mathbf{x} - \omega t)\right] = \mathbf{E}_0 e^{-k\mathbf{k}_0 \cdot \mathbf{x}} \exp\left[j(n\mathbf{k}_0 \cdot \mathbf{x} - \omega t)\right]$$
(2)

Here k_0 is the wave vector, \mathbf{x} is the position of interest in space, ω is the angular frequency of the electromagnetic wave, and \mathbf{E}_0 is the amplitude of the electromagnetic wave. As we can see, due to the imaginary part of the refractive index, $\exp(-k\mathbf{k}_0 \cdot \mathbf{x})$, which is an exponential decay term, appears which indicates that light cannot propagate inside the material since the power reduces so quickly to zero. Therefore, material with an imaginary refractive index is nontransparent. And for those materials that have imaginary

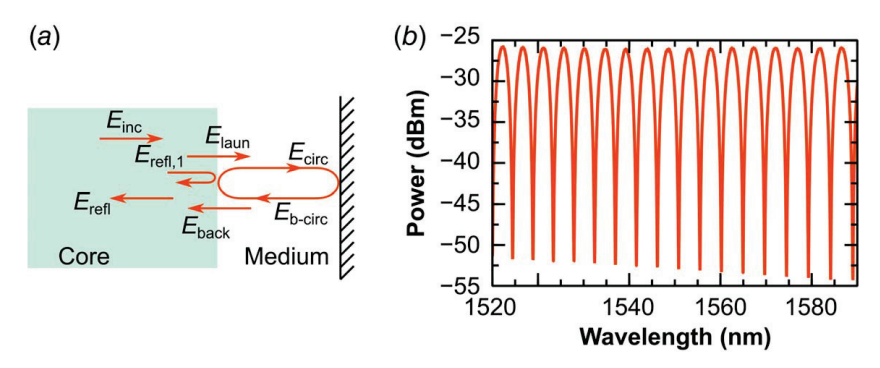


Fig. 3 Light propagation of the fiber optic FPI: (a) working principle of an FPI and (b) a typical reflection spectrum of an FPI

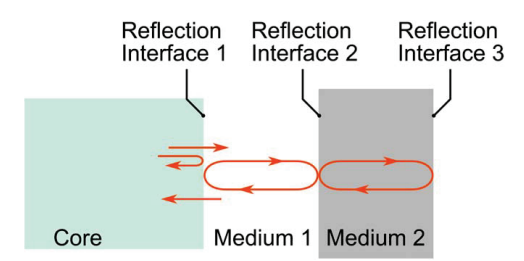


Fig. 4 Cascaded FPI formed by three reflection interfaces

refractive indices of zero are transparent. Figure 5 shows the complex refractive index of silicon. From Fig. 5(a), we can see the imaginary refractive index is not zero in UV and visible range. Figure 5(b) shows a detailed refractive index in the visible range. As we can see, although the imaginary refractive index reduces along the longer wavelength direction in the visible range, it is still not zero. This is the reason that wafer is nontransparent in visible range. However, in the near infrared (NIR) range, with a wavelength greater than 1100 nm, the imaginary refractive index reduces to zero and therefore wafer is transparent in the corresponding wavelength range. In this research, laser with a wavelength of 1550 nm which is inside the transparent range will be used for the monitoring.

Figure 6(a) shows the setup to monitor the upper surface topography and the thickness of the wafer. To form this cascaded FPI, an optical fiber was fixed with its axis perpendicular to the surface of the wafer. A gap was left between the fiber tip and the wafer surface. Therefore, the interface between the fiber tip and air forms the first FPI, and the upper surface and the lower surface form the second FPI. To scan the entire surface, the wafer was held on a six-axis

hexapod (ALIO hybrid hexapod). The wafer was spun along the axis perpendicular to the wafer surface with a constant line speed of the point to be detected with respect to the optical fiber. Meanwhile, the stage also moved perpendicular to the spin axis at a constant line speed. During the monitoring process, the optical fiber did not move with the hexapod. The distance between the fiber tip and the upper surface of the wafer was carefully adjusted before measurement so that the interference spectrum caused by the corresponding FPI can be easily distinguished from that caused by the FPI formed by the wafer. Figure 6(b) shows a section of typical interference spectrum obtained during the monitoring process between 1520 nm and 1530 nm (full wavelength range: 1510-1590 nm). As we can see, the spectrum is a combination of two Airy distributions with distinguishable free spectrum ranges. It is easy to find out which spectrum component is caused by the wafer by adjusting the distance between the fiber and the wafer surface. When the spectrum component shows no change during the movement, that one is caused by the wafer since its thickness will not be changed. And the one that changes is caused by the FPI formed by the fiber tip and the upper wafer surface. The spectrum analysis method was introduced in our previous research [23]. The reciprocal fast Fourier transform (RFT) of the spectrum of the cascaded FPI was taken with an estimation of the optical thickness of the wafer known beforehand. In this research, the geometric thickness of the wafer was estimated between 490 µm and $540 \,\mu\mathrm{m}$ based on the tolerance given by the vendor $(525 \pm$ $10 \mu m$) with a refractive index of 4.00 at 1550 nm. The optical distance between the fiber and the wafer was intentionally set below $500 \,\mu\mathrm{m}$ so that it can be distinguished from the optical thickness of the wafer (from 1703.1 μ m to 1876.9 μ m). Therefore, after taking the RFT, two distinguishable peaks in the optical distance -amplitude plot, which give the optical distance between the fiber and the wafer and that between the two wafer surfaces, can

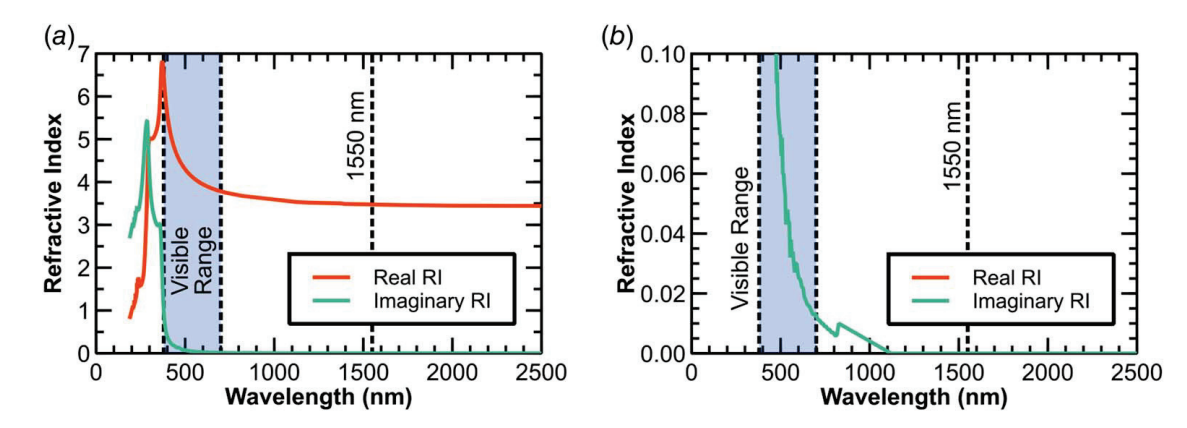


Fig. 5 Real and imaginary refractive indices of silicon: (a) real and imaginary refractive indices of silicon and (b) detailed imaginary refractive index in visible and near infrared regions

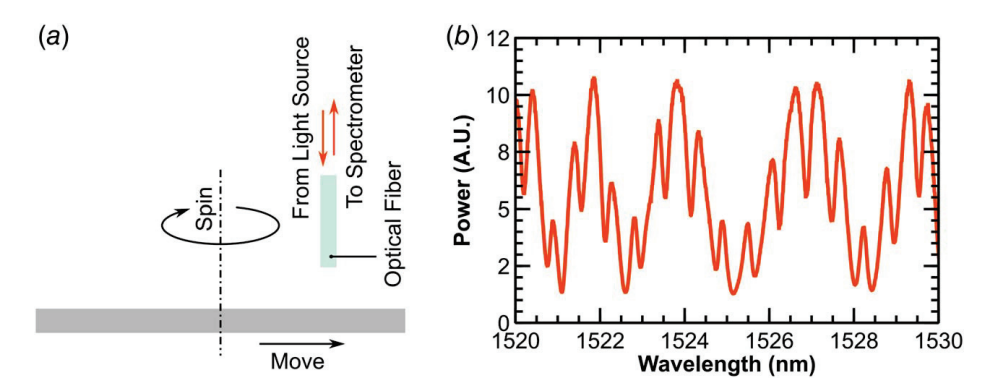


Fig. 6 A typical spectrum of the cascaded FPI acquired during the experiment: (a) schematic drawing of the monitoring system and (b) an experimental spectrum of the FPI

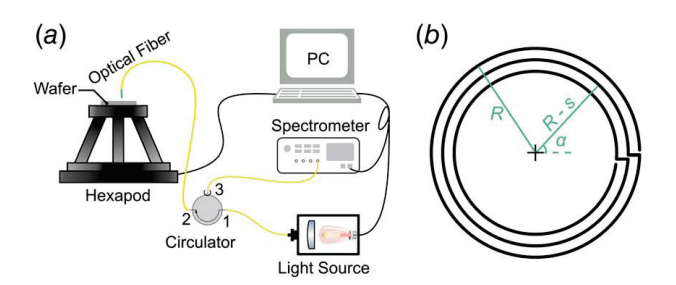


Fig. 7 System connection for wafer profile reconstruction: (a) schematic drawing of the wafer thickness monitoring system and (b) the scan path of the FPI

be seen. Combined with the cross-correlation (xCor) method, the optical distances can be calculated with a resolution of nanometer scale. Here, we ignore the dispersion of air and silicon between 1510 nm and 1550 nm since the change is insignificant.

Figure 7(a) shows the connection of the monitoring system. An optical circulator (Circulator) is a device that light will be guided to port 2 when input from port 1 and will be guided to port 3 when input from port 2. The detection light was generated by a broadband light source (Light Source) covering from 1510 nm to 1590 nm. The light was guided by an SMF to port 1 of the optical circulator. Therefore, the detection light will be guided to the wafer as the input of the cascaded FPI. Then, the reflection light of the cascaded FPI will propagate along the opposite direction in the optical fiber to port 2 and exit from port 3. The light from port 3 will be guided to a spectrometer (Spectrometer) and analyzed by PC. Figure 7(a) shows the scan path during the monitoring process. The wafer was spun along its axis perpendicular to the wafer surface. After each cycle of spin, the wafer was shifted toward the center for a small distance and then spun for the next cycle. From the interference spectrum, we can back calculate the distance between the fiber tip and the upper wafer surface as d(x, y) and the thickness of the wafer as t(x, y). With knowing the rotation angle α , the movement of wafer s, and the distance from the starting point to the center of the wafer R the coordinate of the scanned point can be known as

$$(x, y) = ((R - s)\cos \alpha, (R - s)\sin \alpha)$$
 (3)

Therefore, the coordinate of the wafer surface can be calculated as

$$\begin{cases} d(x, y), & \text{coordinates of upper surface} \\ d'(x, y) = d(x, y) - t(x, y), & \text{coordinates of lower surface} \\ t(x, y), & \text{thickness} \end{cases}$$

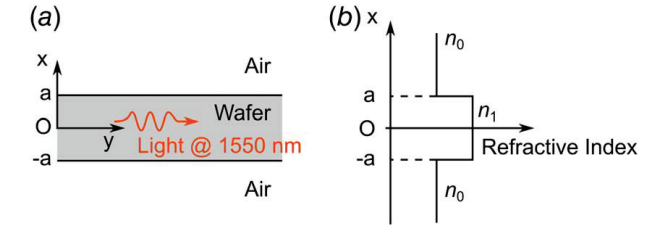


Fig. 8 Wafer as a slab waveguide to guide light at 1550 nm: (a) light propagating in the wafer and the coordinate system and (b) refractive index profile of the core (wafer) and the claddings (air)

2.2 Internal Defect Detection. Systems to inspect the surface quality of wafers have been well developed and can be easily achieved using optical methods such as dark field microscopy, scattering, etc. However, detection of internal defects still relies on bulky and expensive equipment such as X-ray equipment. Since wafer is transparent for light at wavelength of 1550 nm, it is possible to detect the internal quality. However, since the defects are always in micro or nano scales, suppressing the background noise becomes important for successful detection. In this section, we will introduce a detection method taking advantage of a small numerical aperture (NA) of optical fiber and the strong bounding of guiding mode of wafer as a slab waveguide as shown in Fig. 8(a). With this method, internal defects such as cracks, voids, material nonuniformity (localized strain, stress, impurity, etc.), can be detected. As an example, we will detect random micro cracks with a width of around 1 μ m on the lower surface of the wafer from above the wafer. Figure 8(b) shows the refractive index distribution of the waveguide, 2a is the geometric thickness of the wafer.

The dispersion equation, which is the governing equation of the electromagnetic wave in a slab waveguide, can be calculated from Maxwell's equations and the boundary conditions of the wafer. Considering the boundary conditions, the tangential continuity of the electric and magnetic fields, the normal continuity of the electric displacement and the magnetic induction fields, since there are no free electric charges and free electric current on the wafer surface, the electric field of TE modes is given by [24]

$$E_{y} = \begin{cases} A\cos(\kappa a - \phi)e^{-\sigma(x-a)}, & x > a \\ A\cos(\kappa x - \phi), & -a \le x \le a \\ A\cos(\kappa a + \phi)e^{\xi(x+a)}, & x < -a \end{cases}$$
 (5)

where κ , σ , and ξ are wavenumbers of the core and the two claddings along the *x*-direction. In this application, both claddings are air and have an infinitely large thickness. *y*-axis is parallel to the surface of the wafer and perpendicular to the light propagation direction. $E_x = E_z = 0$ for TE modes in a slab waveguide. To

determine the unknowns, use the dispersion equations

$$\begin{cases} w = u \tan\left(u - \frac{m\pi}{2}\right), & m = 0, 1, 2, 3, \dots \\ \phi = \frac{m\pi}{2} \end{cases}$$
 (6)

where u, w are normalized transverse wavenumbers, and $u^2 + w^2 = v^2$. v is the normalized frequency and is determined by the structure of the waveguide

$$v = \frac{2\pi a}{\lambda_0} \sqrt{n_1^2 - n_0^2} \tag{7}$$

Considering the relationship

$$\begin{cases} u = \kappa a \\ w = \xi a \\ w' = w = \sigma a \end{cases}$$
 (8)

Substitute κ , ξ , and σ into Eq. (5) and the electric field of TE modes can be determined. For the electric field of TM modes, a similar process with letting $B_x = B_z = 0$ can be used. Equation (8) has multiple solutions since m can take non-negative integers. mis called the mode order and the corresponding quotation of propagation constant and wavenumber in vacuum is called the effective refractive index which describes the propagation of light in the slab waveguide. Figures 9(a) and 9(b) show the electric field E_{ν} of the TE modes in a slab waveguide (wafer, $x = 0 \mu m$ to $x = 500 \,\mu\text{m}$) with different effective refractive indices n_{eff} . As we can see, the electric field oscillates inside the wafer and decays to zero quickly for both cases. This indicates that light propagation along the slab waveguide (wafer) is bonded inside the wafer and there is no leakage to the far field out of the wafer. This guarantees a low background noise since the detection light cannot be detected when no defects exist in the wafer. The light which is bounded inside the wafer with order number m is called the guiding mode with order m. The light field which decays in the air is called the evanescent field which does not dissipate energy into the air. The evanescent field only exists out of the wafer surface for a distance with a scale of the wavelength of the guiding light. Therefore, for a guiding mode propagate in a slab waveguide (wafer), no light should be detected in the far field perpendicular to the surface of the wafer [25].

However, if there are defects that exist inside the waveguide, the guiding mode can be coupled to the leaky mode and light can escape from the wafer to the space through the wafer-air interface. When light hits the defect, it will be scattered toward all directions. Figure 10 shows an example of light scattered by a void with a diameter of 100 nm inside a wafer using Mie scattering theory. The scattering angle is the difference between the angle of the incident light and the light scattered by the void. As we can see, light is scattered to all the directions with an intensity be a function of scattering angle. Therefore, the scattered light that has an angle with the norm of the wafer surface smaller than the critical angle of total internal reflection will no longer satisfy the guiding requirements. This portion of light will escape from the wafer to the air and becomes the leaky field through the wafer-air interface and therefore can be detected in the far field in the air. So, by measuring the leaky field from the wafer can detect the defects inside it. When no defect exists, the light is tightly bonded inside the wafer and cannot be detected in the far field. Hence, the background noise is also suppressed to a low level.

Figure 11 shows a drawing of the internal defect detection system of the wafer. As we can see, two beams of light source at a wavelength of 1550 nm were guided into the wafer by two SMFs (Lead-In Fiber 1 and Lead-In Fiber 2), which were connected to the laser source, from the wafer edge. A multimode optical fiber (Detection Fiber) was fixed above the wafer surface with a distance between the fiber tip and the surface of ~1 mm. The detection fiber was connected to an optical power meter to measure the optical power which was received by the detection fiber from above the wafer surface. The wafer was spun along its axis perpendicular to the wafer surface and moved along the horizontal direction. The detection fiber was fixed so that it would not move with the wafer. The two lead-in fibers move with the wafer but would not spin. Therefore, the entire surface of the wafer can be scanned, and the internal defects can be detected.

To fix the two lead-in fibers on the hexapod, two fixtures were designed that allow four degrees-of-freedom (horizontal, vertical, roll, and pitch) movement so that the position of the fiber tip can be adjusted for a better alignment. Figure 12 shows the design of a fixture and the lead-in fiber fixed on it. The lead-in fiber was packaged and fixed in a fiber clamp (Fiber Clamp) and the fiber clamp was installed inside the fiber clamp house (Clamp House). The two bolts on the back of the fiber clamp house (Back Bolts) allow

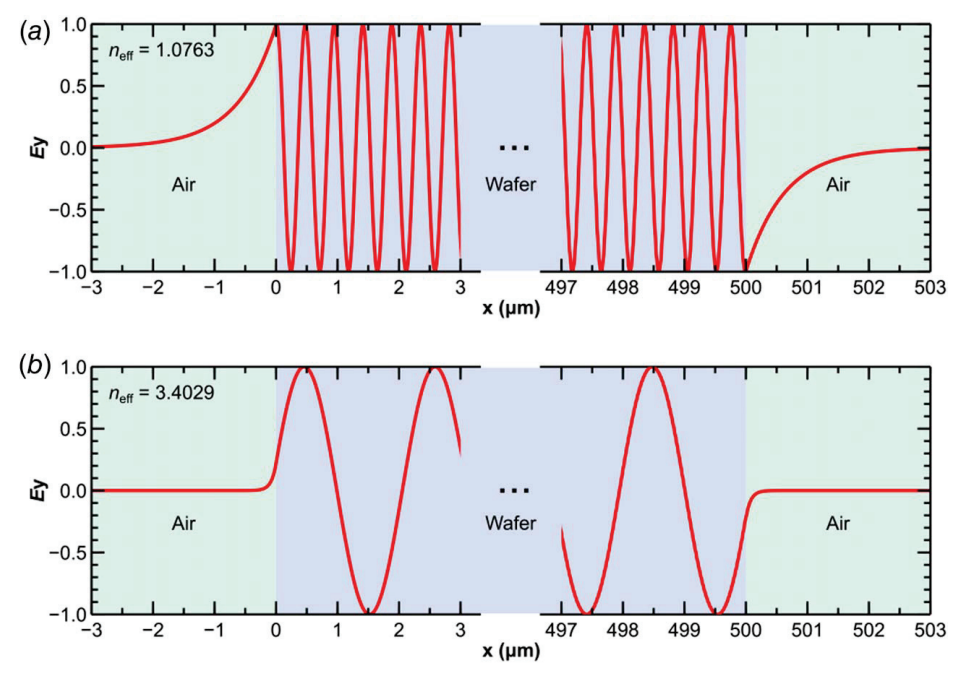


Fig. 9 Supported electric field in a wafer of (a) a higher order mode and (b) a lower order mode

25

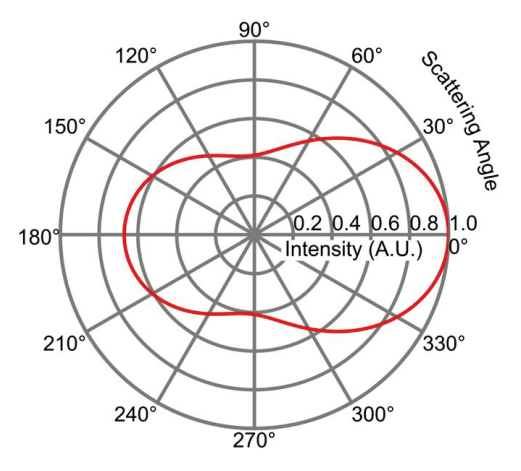


Fig. 10 Light scattered by a spherical void with a diameter of 100 nm in a wafer

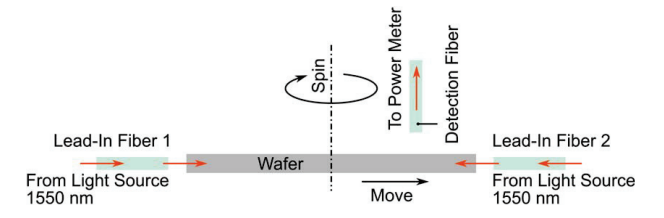


Fig. 11 Schematic drawing of the internal defect detection system

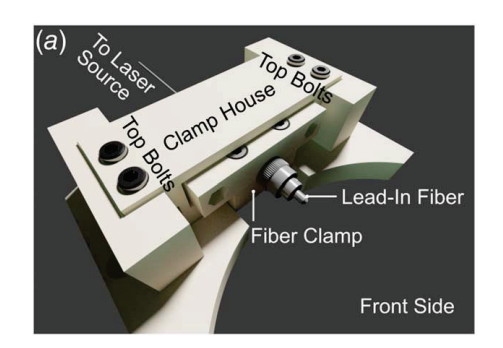
the clamp to move along the horizontal direction. The four bolts on the top of the fiber clamp house (Top Bolts) allow adjustment of the height, roll, and the pitch of the fiber. Since the detection light is in the invisible range, it is recommended to use a visible laser to align the lead-in fibers and the wafer edge. During the monitoring process, the power from the power meter, the coordinates of the wafer, and the timestamp were recorded to reconstruct the defection distribution in the wafer.

Since it is difficult to introduce defects inside the wafer, we ablate marks using femtosecond laser on the lower surface of the wafer when detection fiber is above the upper surface. Figure 13(a) shows the schematic drawing of the femtosecond laser machining system. The laser beam emitted from the femtosecond laser (CARBIDE, wavelength = 515 nm, pulse duration = 229 fs, attenuator = 45%, PP divider = 4, negative chirp) was expanded by a beam expander (Thorlabs, BE02-25-B) to reduce the power density. Then the beam passed an external attenuator to further adjust the power of the laser. An electronic controlled mechanical shutter was used for easier control of the on/off state of the laser power. Mirrors were used to adjust the path of the laser and dichroic mirror which has a high reflectivity of light at 515 nm and a high

transmissivity of other wavelengths was used to reflect the laser and meanwhile allows the camera to monitor the machining process. A 20X objective lens (Mitutoyo, 0.42 NA) was used to focus the laser beam on the lower surface of the wafer. It should be noted that the lower surface of the wafer here is the surface that faces the lens in Fig. 13(a). We call this surface "the lower surface," as shown in the inset of Fig. 13(a), because during defect detection process, this surface will be placed facing the ground so that the defects cannot be seen from above the wafer in the visible range where detection fiber locates. The wafer was fixed on a hexapod (ALIO hybrid hexapod) with a sub micrometer scale positioning accuracy. The wafer was moved by the hexapod with a speed of 1 mm/s and therefore marks were created on the wafer surface with a line width of $\sim 1 \mu m$. Figure 13(b) shows the marks ablated on the lower surface of the wafer. Since we will detect from upper surface, a mirror image of "PURDUE" was ablated for an easier evaluation of the accuracy of the detection results. The patterns around "PURDUE" were ablated by letting the hexapod move along random paths. And Fig. 13(c) shows the mirror image of the ablated mark shown in Fig. 13(b), which should be the pattern that will be detected by detection fiber from above the wafer. Therefore, if the marks on the lower surface can be detected, the defects inside the wafer should be detected as well.

3 Results and Discussion

3.1 Measurement Accuracy Test of Fabry-Pérot **Interferometer.** Although it is unnecessary to calibrate the sensor since the interference spectrum provides the optical distance of the two reflection surfaces directly, the accuracy test was still implemented here for confirmation. According to Eq. (1), the spectrum is a function of optical distance between the two reflection surfaces. Therefore, there are three ways for accuracy test: (1) changing the geometric distance between the two reflection surfaces; (2) changing the refractive index of the medium between the two reflection surfaces; (3) changing both refractive index and geometric distance. Since the sensor has a resolution of nanometer scale, it will be easier to use method (2) since a nanometer scale movement is difficult and vulnerable to ambient noise such as thermal fluctuations and vibrations. To tune the refractive index, sucrose solutions with different concentrations were used since it has been widely used for sensor calibrations and its accuracy has been proved in our previous research [7]. Figure 14 shows the setup for the accuracy test, the sensor was immersed in the sucrose solution and the spectrum was provided by the spectrometer. The inset shows the detailed structure of the fiber optic FPI. The optical fiber was fixed on a piece of glass substrate using epoxy. The optical fiber was fed through a glass ferrule to reduce the influence of vibration. A reflector was installed with its reflection surface perpendicular to the axis of the optical fiber so that the surface of the fiber tip and the surface of the reflector form an FPI. Before the test, the geometric distance between the fiber tip and the reflector should be known in advance. The method is measuring its optical distance using



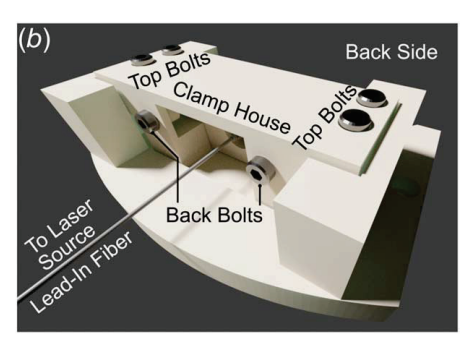


Fig. 12 Design of lead-in fiber holder: (a) front side and (b) back side

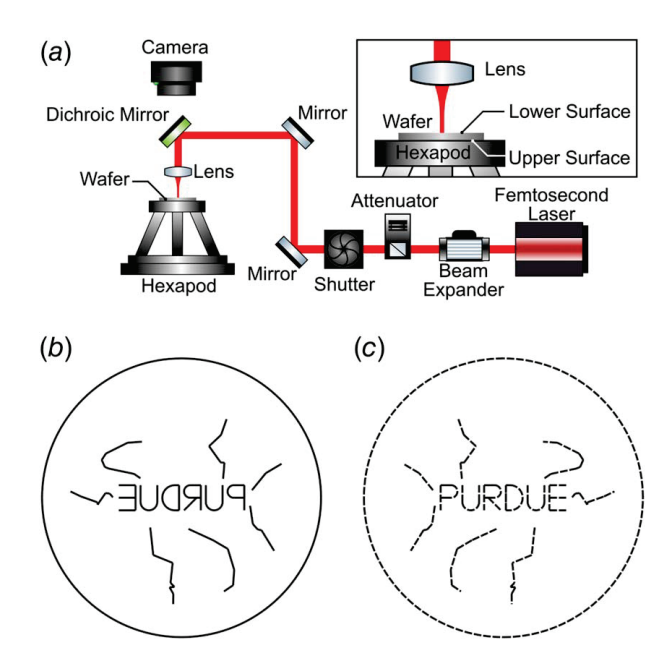


Fig. 13 Laser machining system to make marks on a piece of wafer and the marks on the wafer: (a) the laser machining system, (b) the ablated pattern on the wafer surface, and (c) the mirror image of the ablated pattern

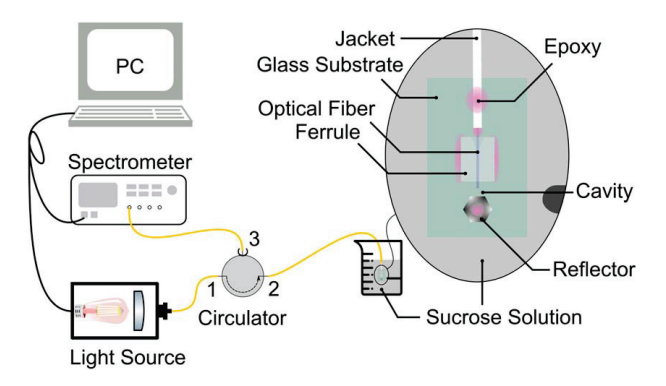


Fig. 14 Setup for the accuracy test by adjusting the refractive index of the solution

the interference spectrum in air. Since the refractive index in air is known as 1.00027326 at 1550 nm [26], the geometric distance can be calculated by dividing the optical distance by refractive index of air. Using this method, the geometric distance was calculated as $387.503 \, \mu \text{m}$. Then, the sensor was immersed in the solution. The refractive index of the sucrose solution was fine-tuned by adding sucrose crystals into the solution so that the mass concentration would be increased by about 0.02% every time. The sucrose was weighted using an analytical balance (US SOLID, model: USS-DBS8) which has a resolution of 0.1 mg. Therefore, it is unnecessary to precisely increase the concentration of the sucrose solution for 0.02% every time since the mass of the sucrose crystal can be measured in a high accuracy and therefore the refractive index increase of the solution can also be calculated with a high accuracy.

Figure 15 shows the testing results including the theoretical optical distance change (labeled as Theo.) and the experimental measurement (labeled as Exp.). As we can see, the experimental test agrees with the theoretical results quite well. At around 10–15 min, there was a data loss because some sucrose particles accidentally got into the space between the fiber tip and the reflector and therefore the spectrum became too noisy to be analyzed.

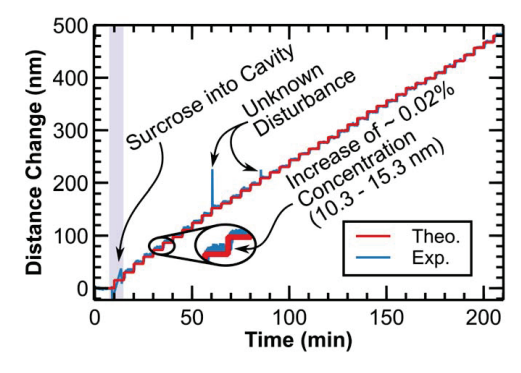


Fig. 15 Accuracy test of the fiber optic Fabry–Pérot interferometer sensor

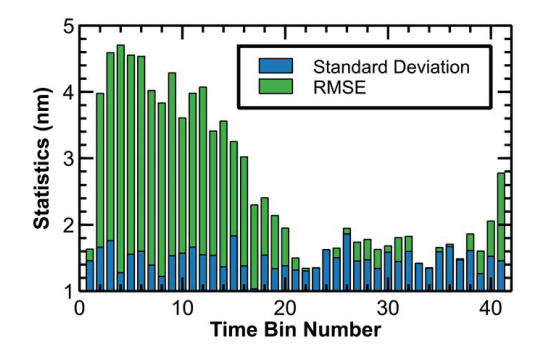
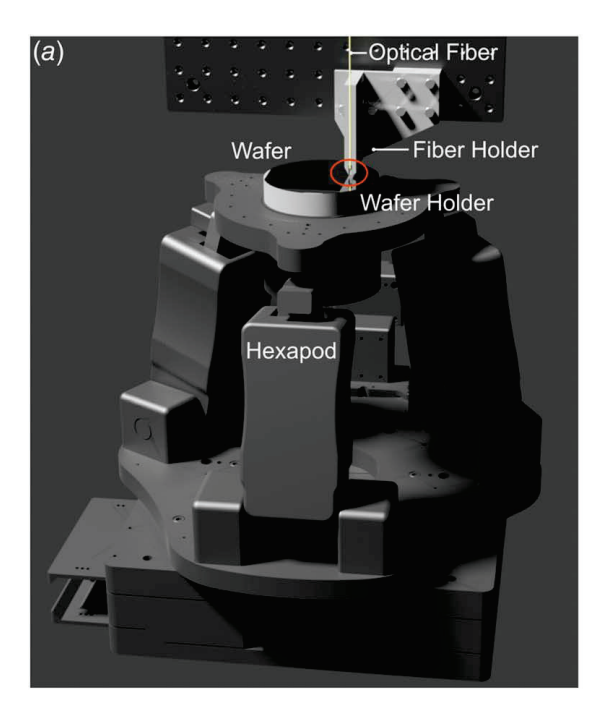


Fig. 16 Accuracy and precision analysis of the measurement

After 5 min, the particles dissolved in the solution and the spectrum recovered and therefore the optical distance was available. This shows the robustness of the sensor since for traditional optical fiber FPIs using a peak-tracking method can easily loss track of the peaks in this case and therefore the measure should be restarted. There were another two outliers that have significantly higher values than expected which could be caused by some unknown disturbance such as a sucrose particle passing through the FPI, or some other reasons, as shown in the figure. But both recovered soon and did not affect the measuring process. The inset shows the details of when the refractive index was increased. As we can see, the experimental and the theoretical results match good.

For a quantitively evaluation of the accuracy and precision, Fig. 16 shows the standard deviation (standard deviation) and the root mean square error (RMSE) of the measurement. The dataset was split into 40 subgroups (time bins) so that each subgroup had a constant refractive index. From time bin 1 to time bin 40, the refractive index increases monotonically as shown in Fig. 15. As we can see, the standard deviation ranges from 1.04 nm to 1.86 nm which shows a precision of less than 2 nm. Also, the distribution of standard deviation is uniform, which shows a constant precision throughout the testing range. Compared with the theoretical result, the RMSE varies from 1.344 nm to 4.705 nm. A relatively high RMSE can be seen between time bin numbers 2 and 20. The possible reason for the higher RMSE may come from the sucrose particle that accidentally entered the FPI as shown in Fig. 15. Although the sucrose particles dissolved quickly, it may cause local concentration changes or a change of the geometry distance between the optical fiber and the reflector if the particle collides with the fiber. Even though the sensor was disturbed, the RMSE is still lower than 5 nm and recovered gradually after 20 time bins. After recovering, most of the RMSE remained lower than 2 nm with only a few between 2 nm and 3 nm. Therefore, the proposed FPI measurement method shows excellent accuracy, precision, and robustness.



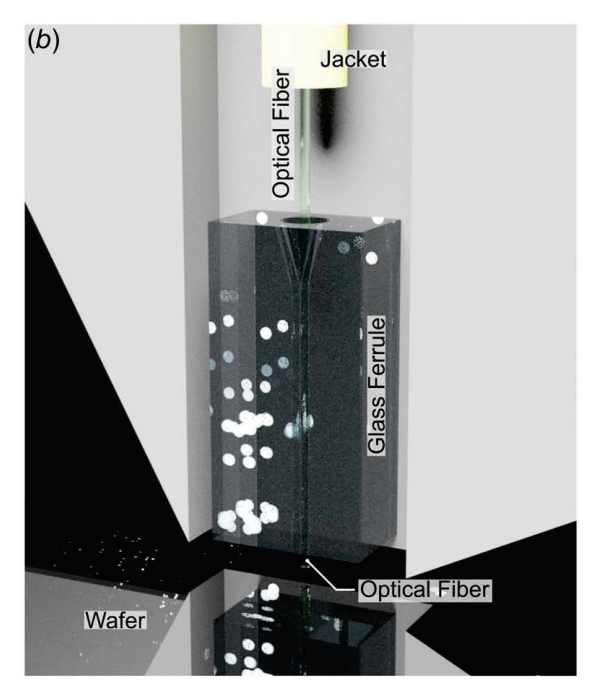


Fig. 17 Wafer 3D profile reconstruction system: (a) the monitoring system and (b) detail of the optical fiber probe

3.2 3D Reconstruction. Figure 17(a) shows the system to reconstruct the 3D profile of the wafer. The wafer holder (wafer holder) was fixed on the top of the hexapod, and the wafer (wafer) was held on the wafer holder. Above the wafer fixed an SMF which was connected to the light source and the spectrometer as shown in Fig. 7(a). During scanning, the wafer was moved with the hexapod and the fiber was kept stationary so that the entire area of the wafer could be scanned. Figure 17(b) shows the detailed drawing of Fig. 17(a) which illustrates the optical fiber probe. The jacket and coating of the SMF were removed and the exposed bare fiber was fed through a glass ferrule to reduce the influence of vibration. The glass ferrule and the optical fiber were bonded on the fiber holder (fiber holder) using epoxy resin. The distance between the optical fiber and the wafer can be determined by observing the interference spectrum from the spectrometer so that the difference between the fringe caused by the wafer and the interface between the fiber tip and the upper surface of the wafer can be distinguished easily as introduced in Sec. 2.1. In this experiment, the distance between the optical fiber and the upper surface of the wafer was set around 150 μ m, which gives a spectrum as shown in Fig. 6.

Figure 18 shows the 3D profile and the thickness of the wafer given by the measurement. The wafer was purchased from ALPHA Nanotech with a thickness of $525 \pm 10 \,\mu m$ as provided by the vendor. Figure 18(a) shows the thickness distribution of the wafer. Here, we assume that the wafer is made of pure silicon, therefore, the refractive index of silicon at 1550 nm at room temperature (3.4757 [27]) was used to calculate geometric thickness of the wafer from its optical thickness. As we can see, the thickness of the wafer ranges from 488 μ m to 504 μ m with a mean of 498.2302 μ m. Compared with the thickness provided by the vendor, there is a difference of $26.77 \,\mu\text{m}$. This difference comes from the refractive index that we used is of pure silicon whereas the wafer is doped with boron. The refractive index of the wafer can be tuned by the type and concentration of the dopants and therefore this information should be known beforehand. For many applications that only interested in the optical thickness instead of the geometric thickness, the dopant will not affect the accuracy since the optical thickness is directly given by the spectrum according to Eq. (1) without knowing extra information of refractive index. The wafer is thicker on the left side, becomes thinner gradually and reaches the lowest value on the right side.

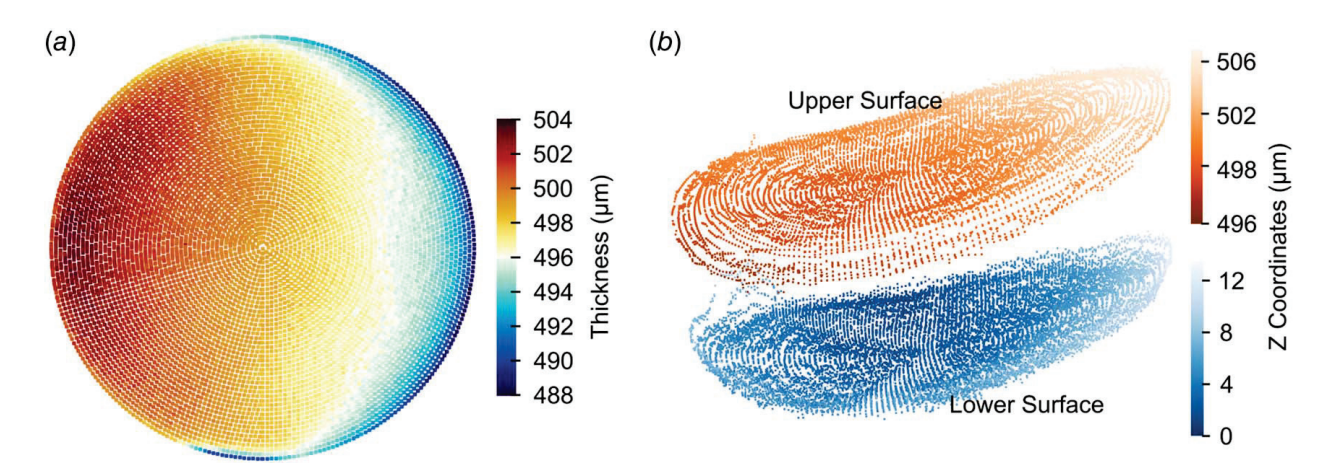
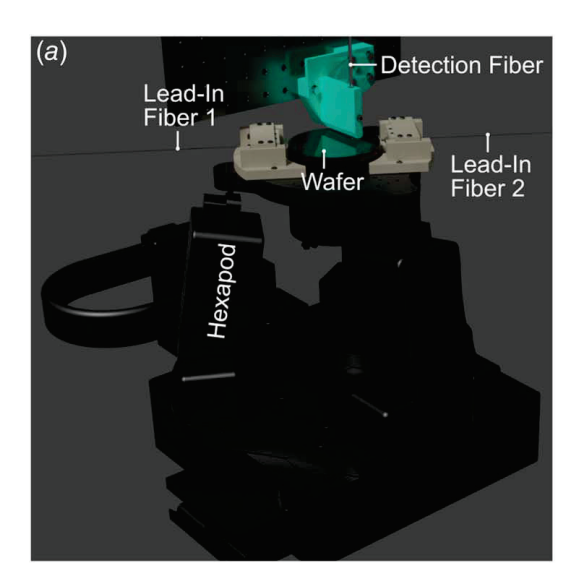


Fig. 18 Reconstruction of its profile (2000 times amplified): (a) the thickness distribution and (b) the reconstructed 3D profile





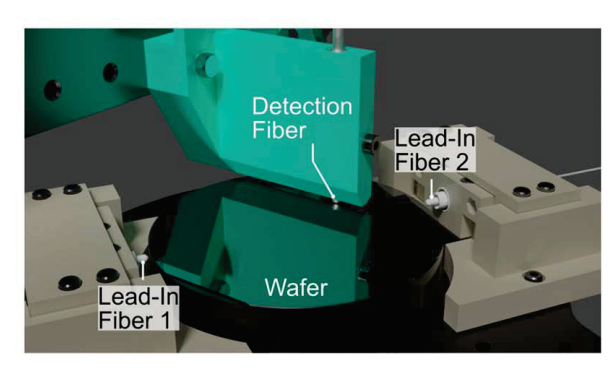


Fig. 19 Internal defect detection system: (a) the monitoring system and (b) the details of the light sources and the scan probe

Figure 18(b) shows the reconstructed 3D profile of the wafer. For a better vision, the profile was amplified 2000 times without scaling the color bar. The distance between the optical fiber and the upper surface of the wafer was calculated according to Eq. (1). Since the refractive index of air was known (1.00027326 at 1550 nm) and the fiber was fixed during the measurement process, the topography of the upper surface is available. Combined with the thickness as shown in Fig. 18(a), the coordinate of the lower surface can be calculated and therefore the 3D profile can be reconstructed. As we can see, the wafer has a wedge shape. The coordinate of the lower surface ranges from $0~\mu m$ to $13~\mu m$ and that of the upper surface ranges from $496~\mu m$ to $507~\mu m$. The wafer exhibits a wrapped topography, which can be caused by the slicing and polishing process.

3.3 Internal Defect Detection. Figure 19 shows the detection system to detect the defect of wafers. A laser diode (LASERSCOM, model: LDI-1550-DFB-2.5G-20/70) with a wavelength of 1550 nm was used as the light source. The operating current and temperature were set as 120 mA and 20 °C, respectively. Therefore, the output of the laser was 20 mW for continuous laser output. The input port of a 3 dB coupler (KS Photonics, fiber variable ratio coupler, working wavelength: 1550 nm) was connected to the output optical fiber of the laser diode so that the laser was split into two beams with equal power. The output ports of the two lead-in fibers were installed at two sides of the wafer with the line that connects the output ports that pass through the center of the wafer. The lead-in fibers were held by two fixtures that have four degrees-of-freedom as introduced in Sec. 2.2. For better coupling efficiency of the laser from the lead-in fibers into the wafer, visible laser with a wavelength of 650 nm was guided into the lead-in fibers before connecting the lead-in fibers to the outputs of the 3 dB coupler. By doing this, the fixtures could be tuned carefully so that the brightest spots of the visible laser from the output ports of the lead-in fibers were on the edge of the wafer. Then, the input ports of the lead-in fibers were connected to the output ports of the 3 dB coupler. A multimode optical fiber/detection fiber (Thorlabs, model: M107L01, working wavelength: 400-2200 nm, NA: 0.50) was fixed above the wafer to detect the leaky field. The multimode fiber was installed with its axis perpendicular to the surface of the wafer. Another port of the multimode fiber was connected to a photon detector (Newport, model: 918D-IG-OD3R, working wavelength: 800-1650 nm) and an optical power meter (Newport, model: 1918-C) for data acquisition.

The distance between the detection fiber and the wafer will affect the signal to noise ratio of the signal. A larger distance will result in a lower power and spatial resolution of the detected leaky field. Therefore, this distance should be determined so that it is close to but will not contact with the wafer surface during the detection process. In this test, the distance between the detection fiber and the wafer surface was set as 1 mm which is enough to detect the leaky field.

Figure 20(a) shows the optical power detected by the detection fiber. For comparison, Fig. 20(b) shows the mirror image of the laser machined pattern on the lower surface as introduced in Sec. 2.2. Ideally, the detected pattern should be the same as Fig. 20(b). In Fig. 20(a), the brighter points are those higher optical power were detected which corresponds to a stronger leaky field. Therefore, the "PURDUE" pattern, which was used for an easier confirmation of the correctness of the detection result, can be clearly observed. It should be noted that since we spun the wafer using a constant line speed at the point to be scanned (below the detection fiber) relative to the detection fiber instead of a constant angular speed, no data were collected on the center of the wafer to avoid an extremely high angular speed. Therefore, the center of Fig. 20(a) is shown as a solid white circle because no data were collected in that region. The random patterns around "PURDUE" can also be observed and show good agreement with Fig. 20(b). At the right side of letter "E" in Fig. 20(a), we can see an area with high intensity of leaky field which is not shown in Fig. 20(b). This is because there are many fine features such as right angles and start/end of lines in this region. These fine features introduced a stronger disturbance of the guided light in the wafer and caused a large number of stray lights which made it easier to escape the wafer. However, despite this leakage of stray light, the pattern of the defect can still be distinguished. And since the leaked stray light is caused by multiple fine features, defects should be expected in this region. It should be noted that the defects caused by laser machining have a line width of around 1 μ m, and the width of the detected pattern is much larger. This is because of the numerical aperture (NA = 0.5) of the detection fiber and the distance between the detection fiber and the wafer. A larger NA means the optical fiber can receive light from environment with a larger angle with respect to the axis of the fiber. Therefore, the leaky light can be detected before and after the detection fiber is right above the defect. This shows an automatic amplification of the defect so that the defects can be easily observed without further treatment. However, this also causes a lower spatial resolution since it will be difficult to distinguish two defects that are very

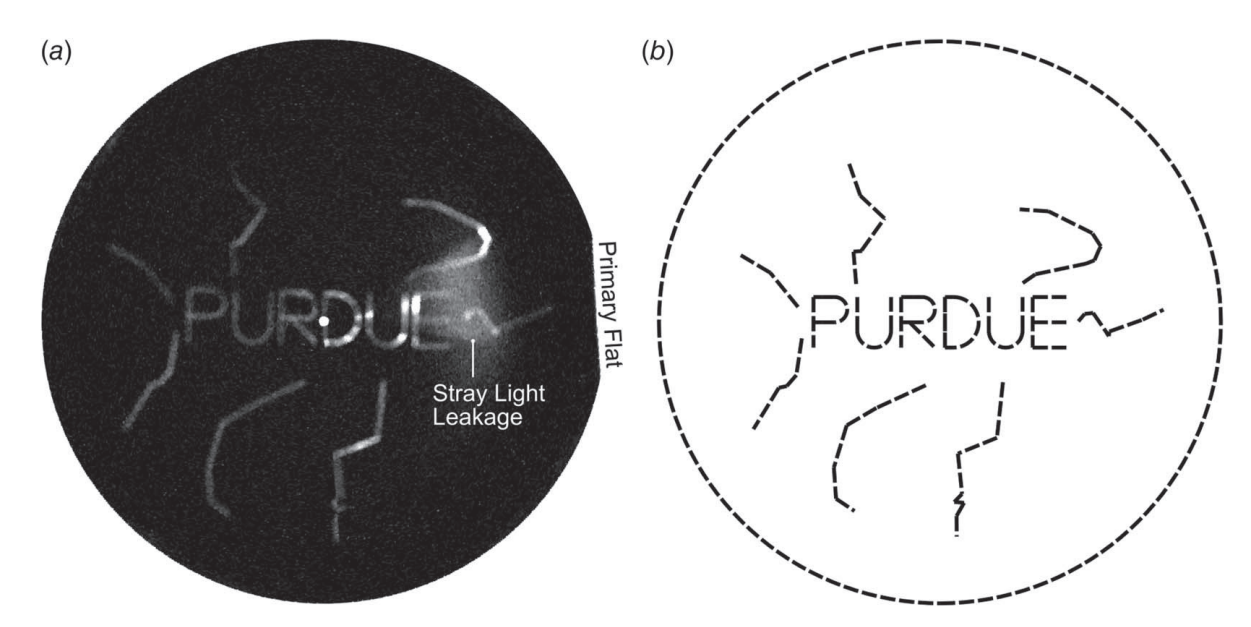


Fig. 20 Defects detected at the bottom surface from the upper surface of the wafer: (a) the detected leaky field and (b) the mirror image of the laser machined pattern

close to each other. To reduce the amplification effect, optical fibers with low NA can be used as detection fiber. Also, detection fiber should be placed as close as possible to the wafer surface. These two parameters should be determined according to the requirement of the detection project.

4 Conclusion

In this research, we introduced the methods of reconstructing the 3D profile of a wafer using cascaded Fabry–Pérot interferometers and detection of defects of a wafer by detecting its leaky field. These applications used the property of the low imaginary refractive index (extinction coefficient) of silicon at near infrared region therefore light can propagate through the wafer. By knowing the 3D profile and the defect distribution, the quality of a wafer can be evaluated. Therefore, the proposed technology has a potential of low-cost evaluation of wafer qualities.

To reconstruct the 3D profile, the topography of the upper surface of a wafer was measured. And the optical thickness distribution of the wafer was measured simultaneously using a cascaded Fabry–Pérot interferometer which was formed by the optical fiber–air interface, upper surface of the wafer, and the lower surface of the wafer. For the geometry distance between the fiber tip and the upper surface of the wafer, it can be calculated easily since the refractive index of air is known and its variation is ignorable. However, the geometric thickness of the wafer can only be determined by knowing its refractive index at the wavelength of the detection light beforehand. The type and the concentration of dopants in the wafer can change the refractive index of the wafer if the wafer is not made of pure silicon, which should be taken into consideration.

To detect the defects in the wafer, especially those inside the wafer that cannot be seen by a simple surface inspection, wafer was treated as a slab waveguide. Two beams of laser at 1550 nm were coupled into the wafer propagating along opposite directions. Since the refractive index of the wafer is much higher than air, the detection light is tightly bonded into the wafer as guiding modes. When defects exist in the wafer, these defects work as scatters which can couple the guiding modes into leaky modes. These leaky modes can be detected at the far field of the wafer by a photon detector. Since the detection light is bonded inside the wafer except defect exists, the sensitivity can be easily improved by increasing the power of the detection light. The experiment

result shows that this method can capture defects with a size of $1\,\mu\mathrm{m}$. For smaller defects, it is still possible to be detected by increasing the power of the detection light or increasing the sensitivity of the photon detector. For a location with multiple fine features such as sharp/right corners, start and end of lines, a leakage caused by a large number of stray lights can be observed. Even though, the defects can still be observed from the noisy background. Moreover, when a leakage of stray light is observed, defects in this region should be expected since the origin of the stray lights is still defects.

Acknowledgment

We acknowledge the support of the National Science Foundation under Grant No. NSF AM-2125826.

Conflict of Interest

There are no conflicts of interest.

Data Availability Statement

The datasets generated and supporting the findings of this article are obtainable from the corresponding author upon reasonable request.

References

- [1] Lu, K., Wang, Z., Chun, H., and Lee, C., 2023, "Curved-Edge Diffractive Fringe Pattern Analysis for Wafer Edge Metrology and Inspection," Metrology, Inspection, and Process Control XXXVII, San Jose, CA, Apr. 27, SPIE, pp. 105–106.
- [2] Chun, H., Wang, J., Kim, J., and Lee, C., 2023, "Wafer Particle Inspection Technique Using Computer Vision Based on a Color Space Transform Model," Int. J. Adv. Manuf. Technol., 127(11), pp. 5063–5071.
- [3] Nishi, Y., and Doering, R., 2000, Handbook of Semiconductor Manufacturing Technology, CRC Press, New York.
- [4] Mayyas, M., Wafer Surface Reconstruction and Characterization for Motion Compensation in a Femtosecond Laser Micromachining System, M.S., The University of Texas at Arlington, TX. https://www.proquest.com/docview/ 305060376/abstract/D89FCB37CC654159PQ/1.
- [5] Sherrington, I., and Smith, E., 1988, "Modern Measurement Techniques in Surface Metrology: Part II; Optical Instruments," Wear, 125(3), pp. 289–308.

- [6] Oh, H.-S., and Lee, H.-L., 2001, "A Comparative Study Between Total Thickness Variance and Site Flatness of Polished Silicon Wafer," Jpn. J. Appl. Phys., 40(9R), p. 5300.
- [7] Zhou, F., Su, H., Joe, H.-E., and Jun, M. B.-G., 2020, "Temperature Insensitive Fiber Optical Refractive Index Probe With Large Dynamic Range at 1,550 nm," Sens. Actuat. A, 312, p. 112102.
- [8] Zhou, F., Fu, X., Chen, S., Kim, E., and Jun, M. B.-G., 2023, "Fiber Optic Sensor for Smart Manufacturing," Int. J. Precis. Eng. Manuf., 1(2), pp. 125–136.
- [9] Joe, H. E., Zhou, F., Yun, S. T., and Jun, M. B. G., 2020, "Detection and Quantification of Underground CO2 Leakage Into the Soil Using a Fiber-Optic Sensor," Opt. Fiber Technol., 60.
- [10] Zhou, F., Jo, S., Fu, X., Tsai, J.-T., and Jun, M. B.-G., 2020, "Fabrication of Optical Fiber Sensors Based on Femtosecond Laser Micro Machining," ASME J. Micro- Nano-Manuf., 8(4), p. 041010.
- [11] Zhou, F., Kung, P., Li, X., Behjat, V., and Jun, M. B. G., 2021, "Modeling of a Sampled Apodized Fiber Bragg Grating Moisture Sensor," Opt. Fiber Technol., 65, p. 102630.
- [12] Su, H., and Zhou, F., 2018, "Optimization of Micro-Optical Fiber-Based Mach-Zehnder Interferometer RI Sensor," J. Lightwave Technol., 36(18), pp. 4039–4045
- [13] Zhou, F., Tsai, J.-T., Jo, S., Kim, G., Lee, P. C., and Jun, M. B.-G., 2020, "In-Situ Monitoring of Solidification Process of PVA Solution by Fiber Optic Sensor Technique," IEEE Sens. J., 21(5), pp. 6170–6178.
- [14] Fu, X., Zhou, F., Yun, H., Kim, E., Chen, S., and Jun, M. B.-G., 2023, "Machine Straightness Error Measurement Based on Optical Fiber Fabry–Pérot Interferometer Monitoring Technique," ASME J. Manuf. Sci. Eng., 145(1), p. 011007.
- [15] Zhou, F., Duan, W., Li, X., Tsai, J.-T., and Jun, M. B. G., 2021, "High Precision In-Situ Monitoring of Electrochemical Machining Process Using an Optical Fiber Fabry–Pérot Interferometer Sensor," J. Manuf. Processes, 68, pp. 180–188.
- [16] You, K. E., Uddin, N., Kim, T. H., Fan, Q. H., and Yoon, H. J., 2018, "Highly Sensitive Detection of Biological Substances Using Microfluidic Enhanced Fabry-Perot Etalon-Based Optical Biosensors," Sens. Actuat. B, 277, pp. 62–68.
- [17] Jiang, M., Li, Q. S., Wang, J. N., Yao, W. G., Jin, Z., Sui, Q., Shi, J., Zhang, F., Jia, L., and Dong, W. F., 2013, "Optical Response of Fiber-Optic Fabry-Perot

- Refractive-Index Tip Sensor Coated With Polyelectrolyte Multilayer Ultra-Thin Films," J. Lightwave Technol., **31**(14), pp. 2321–2326.
- [18] Butt, M., Khonina, S., and Kazanskiy, N., 2019, "Numerical Analysis of a Miniaturized Design of a Fabry-Perot Resonator Based on Silicon Strip and Slot Waveguides for Bio-Sensing Applications," J. Mod. Opt., 66(11), pp. 1172-1178.
- [19] Miguel-Sánchez, J., Reinhard, A., Togan, E., Volz, T., Imamoglu, A., Besga, B., Reichel, J., and Estève, J., 2013, "Cavity Quantum Electrodynamics With Charge-Controlled Quantum Dots Coupled to a Fiber Fabry-Perot Cavity," New J. Phys., 15(4), p. 045002.
- [20] Pfeifer, H., Ratschbacher, L., Gallego, J., Saavedra, C., Faßbender, A., von Haaren, A., Alt, W., et al., 2022, "Achievements and Perspectives of Optical Fiber Fabry–Perot Cavities," Appl. Phys. B, 128(2), p. 29.
- [21] Srinivasan, K., and Painter, O., 2007, "Linear and Nonlinear Optical Spectroscopy of a Strongly Coupled Microdisk-Quantum Dot System," Nature, 450(7171), pp. 862–865.
- [22] Ismail, N., Kores, C. C., Geskus, D., and Pollnau, M., 2016, "Fabry-Pérot Resonator: Spectral Line Shapes, Generic and Related Airy Distributions, Linewidths, Finesses, and Performance at Low or Frequency-Dependent Reflectivity," Opt. Express, 24(15), pp. 16366–16389.
- [23] Zhou, F., Chen, S., Fu, X., and Jun, M. B. G., 2024, "Real-Time Monitoring of the Interelectrode Gap During Electrochemical Machining Processes Using a Smart Machine Tool Equipped With an Optical Fiber Fabry-Pérot Interferometer: Principle and Application," Mech. Syst. Signal Process, 211, p. 111245.
- [24] Okamoto, K., 2006, Fundamentals of Optical Waveguides, Academic Press, Burlington, MA.
- [25] Pitilakis, A., and Kriezis, E. E., 2022, "Ultrafast Pulse Propagation in Graphene-Comprising Nanophotonic Waveguides Considering Nonperturbative Electrodynamic Nonlinearity," J. Opt. Soc. Am. B, 39(10), pp. 2723–2734.
- [26] Ciddor, P. E., 1996, "Refractive Index of Air: New Equations for the Visible and Near Infrared," Appl. Opt., 35(9), pp. 1566–1573.
- [27] Li, H. H., 1980, "Refractive Index of Silicon and Germanium and Its Wavelength and Temperature Derivatives," J. Phys. Chem. Ref. Data, 9(3), pp. 561–658.